Supplementary Materials

Beyond Lithium Paradigms: Distinct Electrochemo-Mechanical Behaviors of Sodium-Ion Batteries

Shijia Xu [1], Yiming Yang [1], Tao Wang [1], Xiaoping Chen [1] *

[1] *Zhejiang Provincial International Joint Laboratory of New Energy Vehicle Technology, College of Mechanical and Automotive Engineering, Ningbo University of Technology, Ningbo, China*

*Corresponding to: Dr. Xiaoping Chen: cxp@nbut.edu.cn

1. Mechanical reproducibility

1.1 Full cell lateral compression

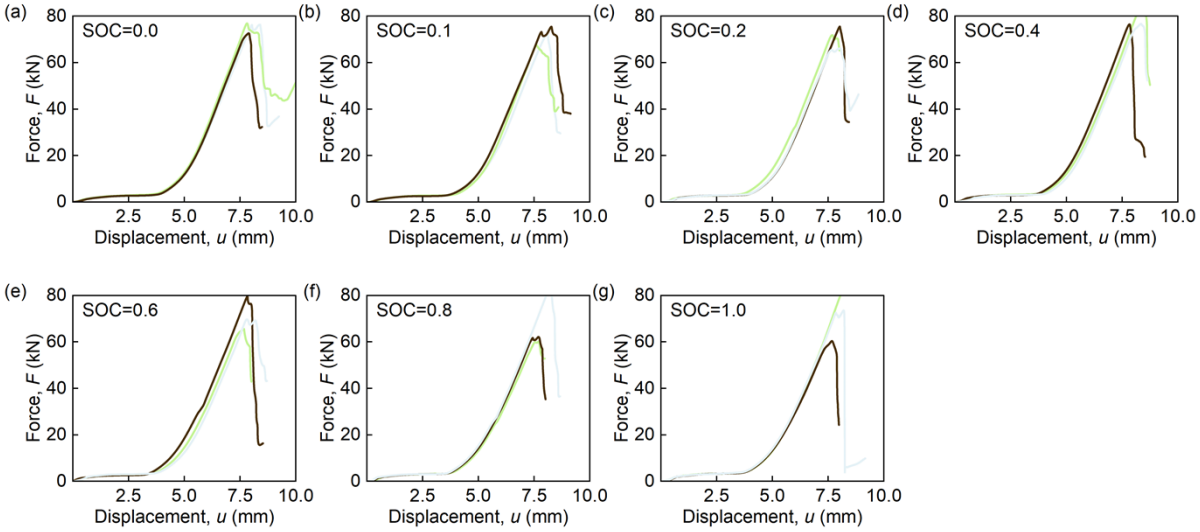

Figure S1. Reproducibility of the mechanical response of commercial 18650 sodium-ion batteries. Force-displacement curves obtained from lateral compression tests at various SOC levels: (a) 0.0, (b) 0.1, (c) 0.2, (d) 0.4, (e) 0.6, (f) 0.8, and (g) 1.0. The highly overlapping curves from independent triplicate tests demonstrate the consistency of the macroscopic mechanical behavior.

1.2 Anode compression

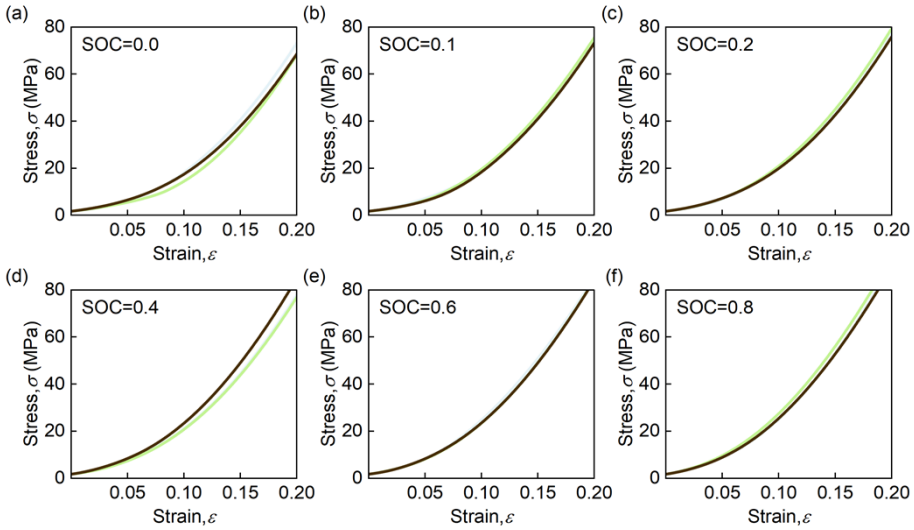

Figure S2. Compressive stress-strain curves of the hard carbon anode at various SOCs. (a–f) Uniaxial compression results for anode stacks at SOCs ranging from 0.0 to 0.8. The curves exhibit high repeatability, validating the subtle SOC-hardening trend discussed in the main

text.

1.3 Cathode compression

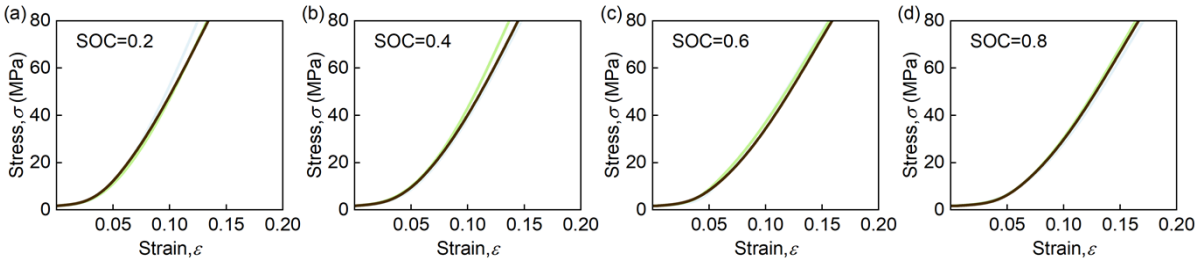

Figure S3. Compressive stress-strain curves of the NFM cathode at various SOCs. (a–d) Uniaxial compression results for cathode stacks at SOCs of 0.2, 0.4, 0.6, and 0.8. The consistent data supports the observation of cathode softening upon desodiation.

1.4 Anode tension

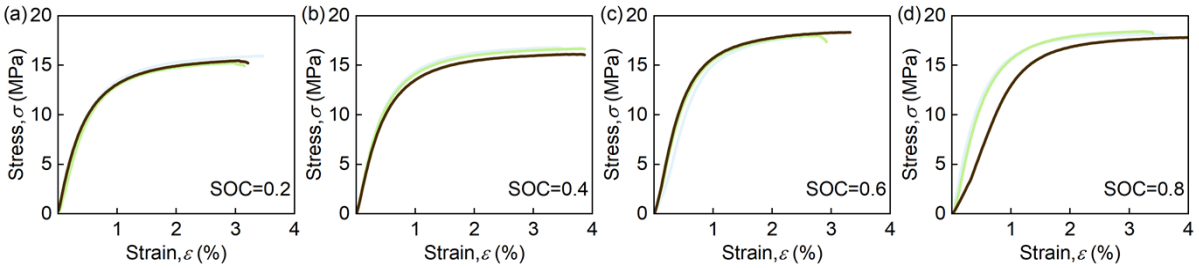

Figure S4. Tensile stress-strain curves of the hard carbon anode. (a–d) Tensile behavior of the anode at SOC 0.2, 0.4, 0.6, and 0.8. The reproducibility of the failure strain (~3.5%) confirms that the anode maintains its ductility and is governed by the current collector's limit across the full SOC range.

1.5 Cathode tension

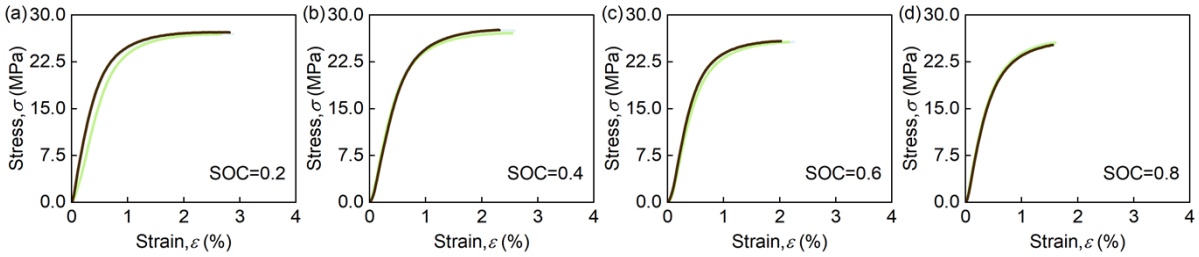

Figure S5. Tensile stress-strain curves of the NFM cathode. (a–d) Tensile behavior of the cathode at SOC 0.2, 0.4, 0.6, and 0.8. The repeated tests confirm the distinct reduction in failure strain at high states of charge.

1.6 Separator tension

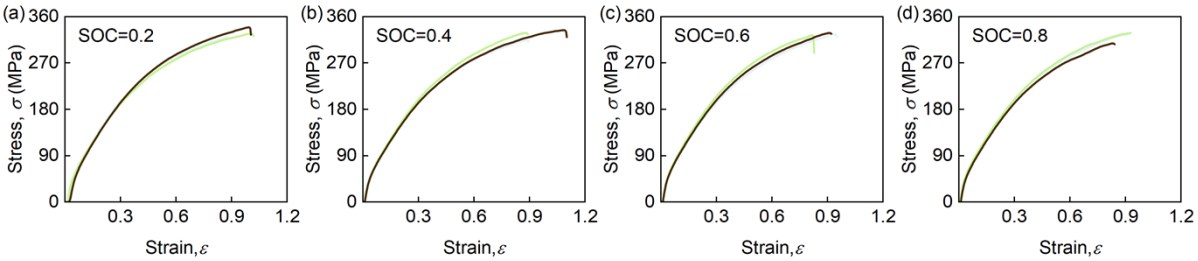

Figure S6. Tensile stress-strain curves of the separator. (a–d) Mechanical response of the separator at different SOCs. The identical curves rule out separator degradation as a variable in the SOC-dependent full-cell failure.

1.7 Casing tension

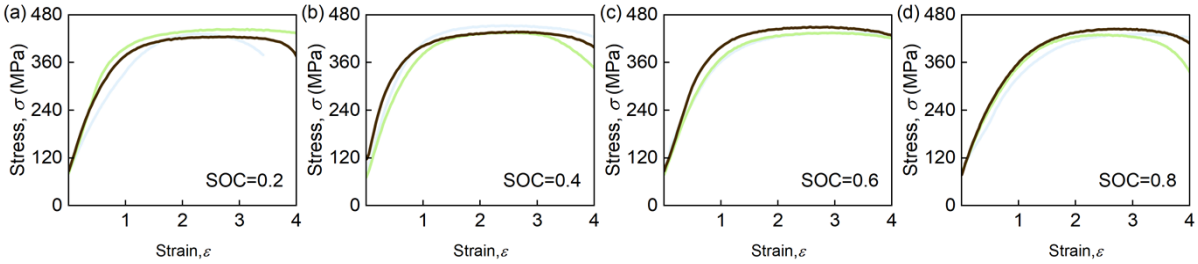

Figure S7. Tensile stress-strain curves of the steel casing. (a–d) Mechanical response of the battery casing material, showing SOC-independent constitutive behavior.

2. *Ex-situ* XRD patterns of the harvested commercial Na-Ni-Fe-Mn-O cathodes

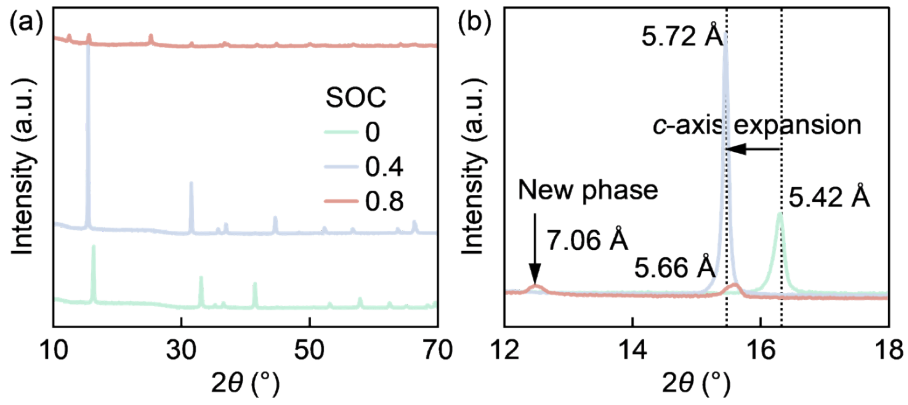

Figure S8. *Ex-situ* XRD patterns of the harvested commercial Na-Ni-Fe-Mn-O cathodes at different states of charge (SOC 0, 0.4, and 0.8). (a) Full XRD spectra. (b) Magnified view of the 12°–18° region, highlighting the dynamic structural evolution of the characteristic diffraction peak. The continuous shift of the main peak to lower angles (from 16.33° to 15.47°) indicates a significant c-axis expansion (from d = 5.42 Å to 5.72 Å) during initial desodiation.

At SOC 0.8, the emergence of a distinct new diffraction peak at 12.53° (d = 7.06 Å) definitively confirms a severe structural phase transition (e.g., from O3 to P3 phase). This massive crystallographic volume variation and phase reconfiguration inherently correlate with the macroscopic mechanical softening of the cathode.

3. Post-mortem cross-sectional SEM images of the fractured hard carbon anode

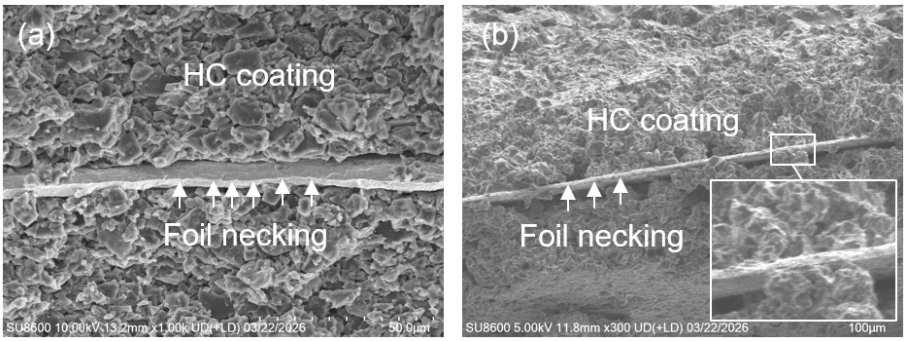

Figure S9. Post-mortem cross-sectional SEM images of the fractured hard carbon (HC) anodes after the tensile tests. (a) The fully discharged state (SOC 0) at high magnification, showing the severe localized plastic necking of the Cu foil. The HC coating tightly conforms to the plastically deformed substrate right up to the fracture tip without interfacial debonding. (b) The highly charged state (SOC 0.8), demonstrating that even after significant sodiation, the HC layer maintains a dense and intact interface with the Cu foil. No premature spallation or macroscopic delamination is observed, unequivocally

4. High-pressure compressive integrity of electrode components

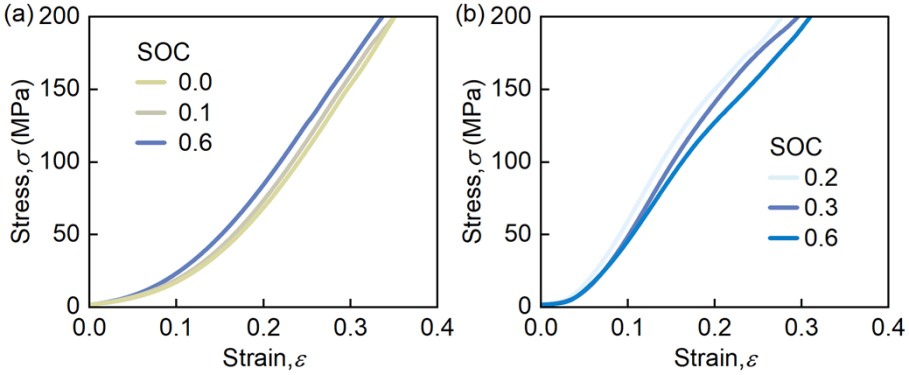

Figure S10. High-pressure compressive integrity of electrode components. Uniaxial compression stress-strain curves of (a) the Hard Carbon anode and (b) the NFM cathode loaded up to 200 MPa at representative SOCs. The curves remain monotonic and smooth without exhibiting any abrupt stress drops or fracture signatures. This confirms that the active material coatings maintain structural integrity under high compressive loads, thereby ruling out compressive crushing as the primary trigger for the internal short circuit.

5. Electrical reproducibility

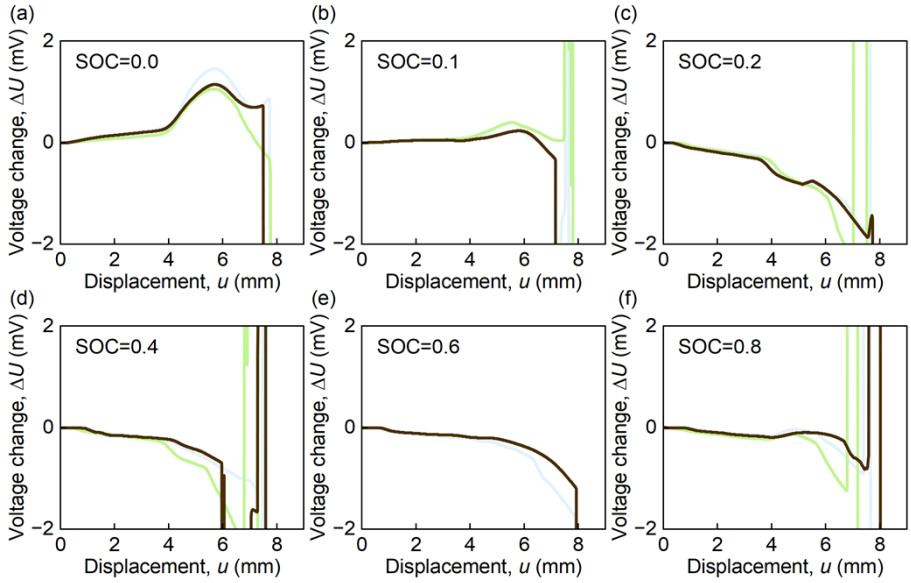

Figure S11. Reproducibility of the mechano-electrochemical voltage response. Voltage variation versus displacement curves corresponding to the mechanical tests in Figure S5. Across all SOCs (a–f), the distinct low-SOC voltage rise and high-SOC voltage drop phenomena are consistently reproduced, confirming that the bifurcation behavior is a stable characteristic of the battery system.

6. *In-situ* EIS evolution across the full SOC range under compression

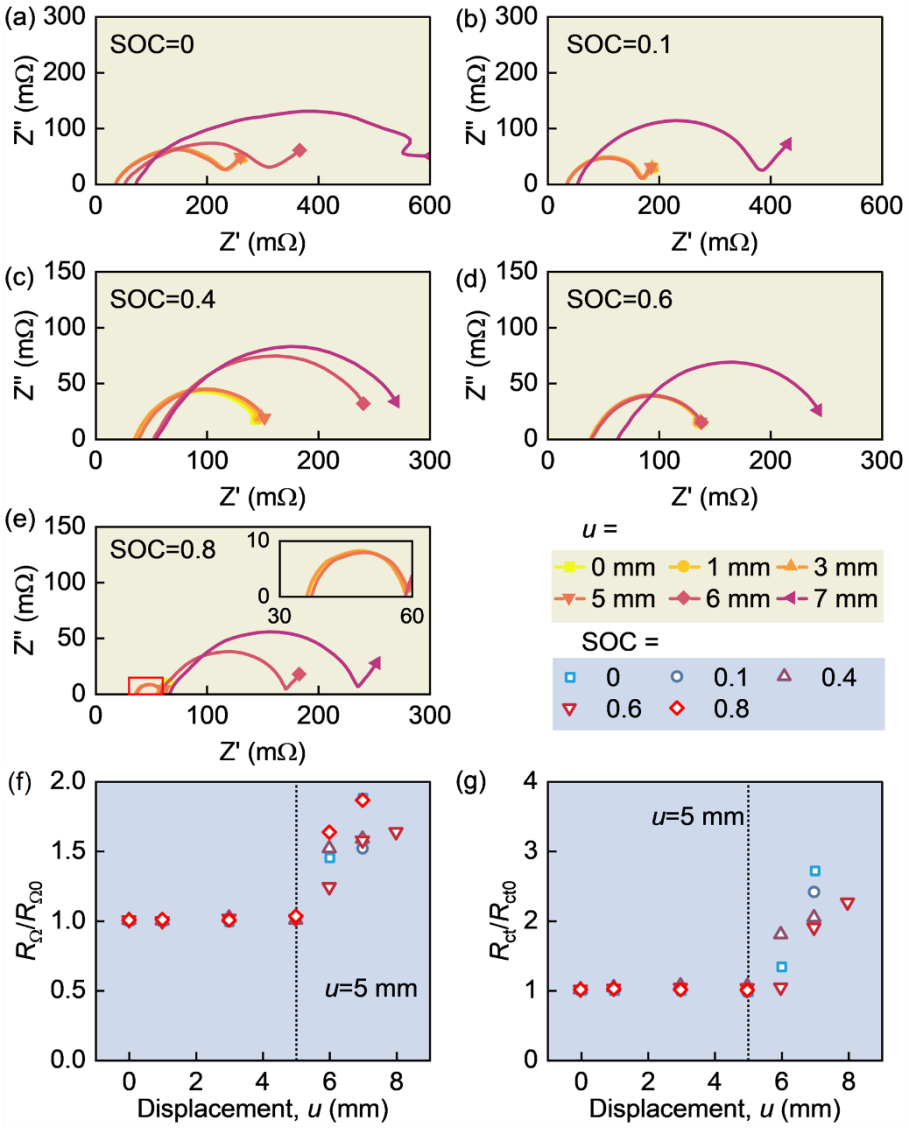

Figure S12. *In-situ* electrochemical impedance spectroscopy evolution of the full cells under progressive quasi-static compression. (a–e) Nyquist plots measured at various states of charge (SOC = 0, 0.1, 0.4, 0.6, and 0.8) under different compression displacements (u ranging from 0 to 7 mm). (f) The normalized ohmic resistance ($R_\Omega/R_{\Omega 0}$) and (g) normalized charge transfer resistance (R_{ct}/R_{ct0}) as a function of the applied displacement u. The vertical dashed line at u=5 mm indicates the critical mechanical threshold, beyond which the internal reaction kinetics experience abrupt deterioration due to structural densification.

7. Time-synchronized evolution of stress and potential

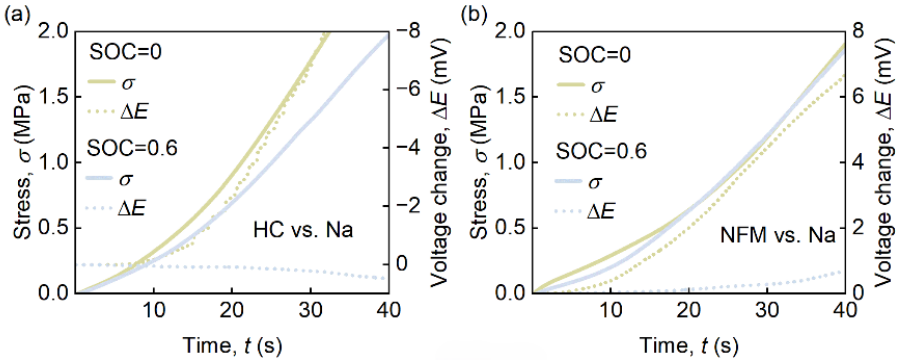

Figure S13. Time-synchronized evolution of stress and potential in half-cell decoupling tests. (a) hard carbon anode (HC vs. Na) and (b) NFM cathode (NFM vs. Na). The potential change (ΔE, dotted lines) tracks the applied compressive stress (σ, solid lines) linearly over time with negligible lag. This synchronous response confirms that the measured potential shift is a direct manifestation of thermodynamic equilibrium changes rather than kinetic polarization or transport delays.

8. Voltage bifurcation phenomenon universality verification

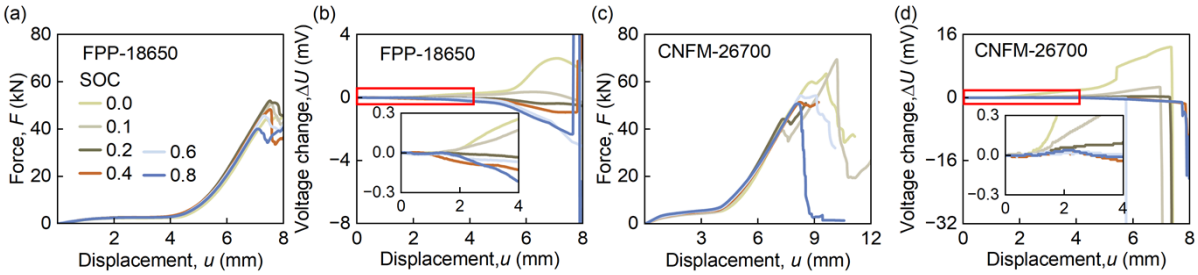

Figure S14. Universality verification of the voltage bifurcation phenomenon across different cell chemistries and formats. (a) Mechanical force and (b) voltage response of FPP-18650 cells (Chemistry: $Na_2FeP_2O_7$ || hard carbon). Despite utilizing a polyanion cathode with minimal volume expansion, still exhibits the identical voltage bifurcation pattern. (c) Mechanical force and (d) voltage response of larger format CNFM-26700 cells (Chemistry: Na ($Ni_xFe_yMn_zCu_{1-x-y-z}$) O_2 || hard carbon). The consistent bifurcation pattern confirms that the thermodynamic stress-potential coupling is a scale-independent material property.

9. Sample preparation and structural characterization

9.1 Full cell CT scan

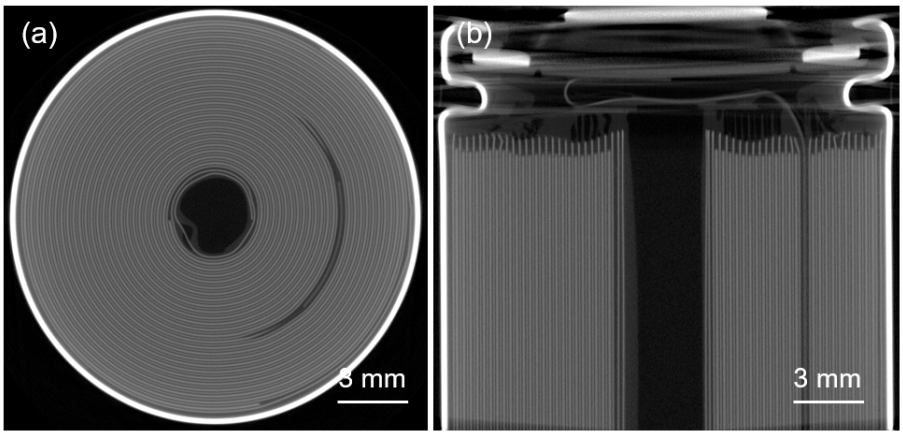

Figure S15. Internal structural inspection of the commercial 18650 sodium-ion battery. (a) Transverse and (b) longitudinal cross-sectional X-ray CT images of the fresh cell. The scans confirm a uniform jellyroll structure and the presence of a central mandrel, verifying the structural integrity of the samples prior to lateral compression testing.

9.2 Electrodes SEM analysis

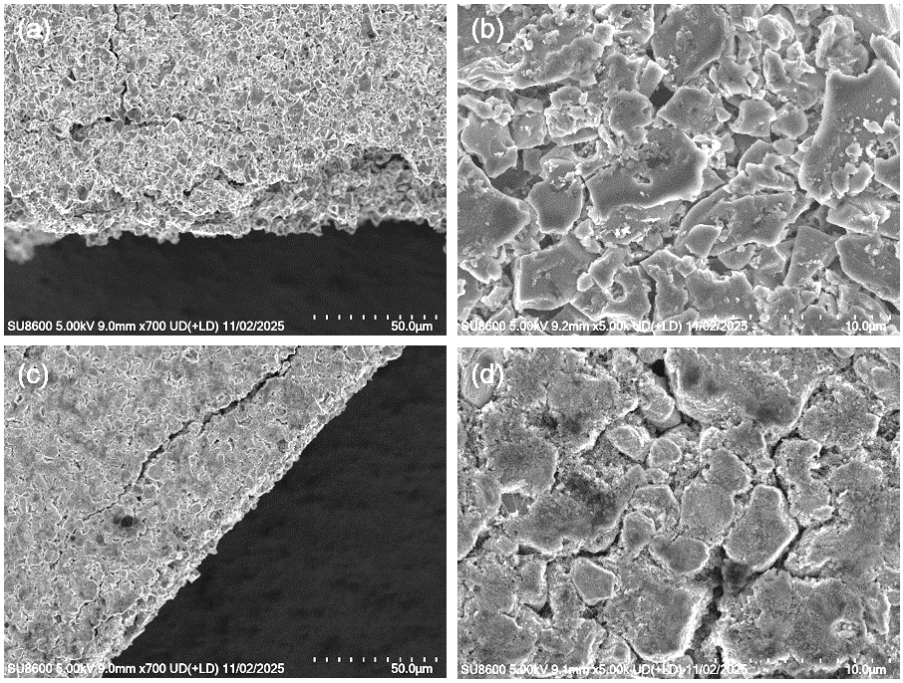

Figure S16. Morphological characterization of the pristine electrode materials (0% SOC). SEM images of (a, b) the hard carbon anode and (c, d) the NFM cathode at low and high magnifications. The images reveal the irregular particle shapes of the hard carbon and the

granular nature of the cathode coating.

9.3 Half-cell CT scan

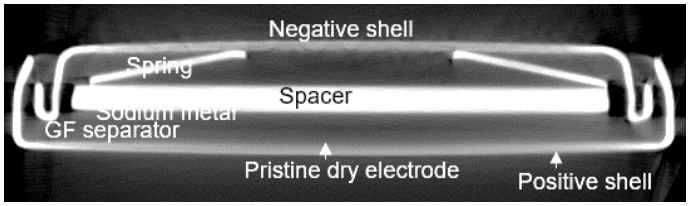

Figure S17. Non-destructive validation of the in-situ half-cell compression fixture via X-ray Computed Tomography (CT). The cross-sectional CT image clearly visualizes the internal alignment of the customized coin-cell assembly.

9.4 Half-cell formation

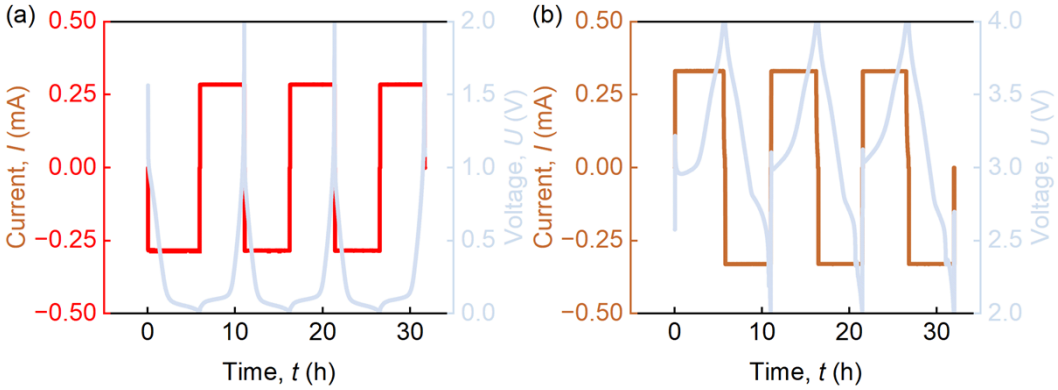

Figure S18. Electrochemical formation profiles of the surrogate half-cells used for decoupling analysis. (a) Voltage-time curve of the Hard Carbon anode half-cell, and (b) Voltage-time curve of the NFM cathode half-cell. The cells underwent a formation protocol of 3 cycles at 0.2 C. The stable and overlapping charge/discharge profiles confirm the successful activation of the electrode materials and the formation of a stable SEI prior to mechanical testing.